Device Performance of the Mott Insulator $LaVO_3$ as a Photovoltaic Material

Lingfei Wang,[1] Yongfeng Li,[2] Ashok Bera,[1] Chun Ma,[1] Feng Jin,[3] Kaidi Yuan,[4] Wanjian Yin,[5] Adrian David,[6] Wei Chen,[4] Wenbin Wu,[3] Wilfrid Prellier,[6] Suhuai Wei,[5] and Tom Wu[1,*]

[1]*Materials Science and Engineering, King Abdullah University of Science and Technology (KAUST), Thuwal 23955-6900, Saudi Arabia*

[2]*Key Laboratory of Physics and Technology for Advanced Batteries (Ministry of Education), College of Physics, Jilin University, Changchun 130012, People's Republic of China*

[3]*Hefei National Laboratory for Physical Sciences at Microscale, University of Science and Technology of China, and High Magnetic Field Laboratory, Chinese Academy of Sciences, Hefei 230026, People's Republic of China*

[4]*Department of Physics, National University of Singapore, 2 Science Drive 3, Singapore 117543*

[5]*National Renewable Energy Laboratory, Golden, Colorado 80401, USA*

[6]*Laboratoire CRISMAT, CNRS UMR 6508, ENSICAEN, 14050 Caen, France*

(Received 13 February 2015; published 22 June 2015)

Searching for solar-absorbing materials containing earth-abundant elements with chemical stability is of critical importance for advancing photovoltaic technologies. Mott insulators have been theoretically proposed as potential photovoltaic materials. In this paper, we evaluate their performance in solar cells by exploring the photovoltaic properties of Mott insulator $LaVO_3$ (LVO). LVO films show an indirect band gap of 1.08 eV as well as strong light absorption over a wide wavelength range in the solar spectrum. First-principles calculations on the band structure of LVO further reveal that the *d*-*d* transitions within the upper and lower Mott-Hubbard bands and *p*-*d* transitions between the O 2*p* and V 3*d* band contribute to the absorption in visible and ultraviolet ranges, respectively. Transport measurements indicate strong carrier trapping and the formation of polarons in LVO. To utilize the strong light absorption of LVO and to overcome its poor carrier transport, we incorporate it as a light absorber in solar cells in conjunction with carrier transporters and evaluate its device performance. Our complementary experimental and theoretical results on such prototypical solar cells made of Mott-Hubbard transition-metal oxides pave the road for developing light-absorbing materials and photovoltaic devices based on strongly correlated electrons.

DOI: 10.1103/PhysRevApplied.3.064015

I. INTRODUCTION

3*d* transition-metal oxides (TMOs) have been extensively studied for decades as one of the most important strongly correlated electronic systems. Because of the rather localized 3*d* orbitals, the electron-electron interaction in these oxides is significant and crucial in determining the physical properties [1,2]. In the widely used Hubbard model, the electron-electron interaction is represented by the on-site Coulomb repulsion U, which opens a Mott-Hubbard energy gap inside the 3*d* band [3]. As illustrated in Fig. 1(a), according to the relative magnitudes of U and the oxygen 2*p*–to–metal 3*d* charge-transfer energy Δ, insulating TMOs can be classified into Mott insulators ($U < \Delta$) and charge-transfer insulators ($U > \Delta$) [4]. By controlling the electron correlation via temperature, chemical and electrostatic doping, pressure, and magnetic and electric fields, a variety of novel phenomena has been observed in these systems, including high-temperature superconductivity [5] and colossal magnetoresistance [6].

Very recently, adding another dimension to the research of TMO, narrow-band-gap Mott insulators were proposed as promising solar-absorbing materials [7–9]. The Mott-Hubbard-type TMOs usually contain only earth-abundant elements and intrinsically have long-term chemical stability, which is suitable for constructing low-cost and durable photovoltaic devices. Moreover, as shown in Fig. 1(b), the Mott and charge-transfer insulators, with different compositions but similar perovskite structures, can offer band gaps ranging from near infrared to ultraviolet (UV) [10–14]. The structure compatibility and wide-range band-gap tunability could potentially enable multijunction solar cells to maximize the solar absorption. Manousakis *et al.* [7,8] theoretically predicted that the strong Coulomb interaction in Mott insulators may trigger the carrier multiplication process; i.e., a single photon efficiently produces multiple electron-hole pairs, thus, increasing the quantum efficiency [7,8]. Most important, such Mott-insulator-based solar-harvesting devices, if realized,

*Corresponding author.
tao.wu@kaust.edu.sa

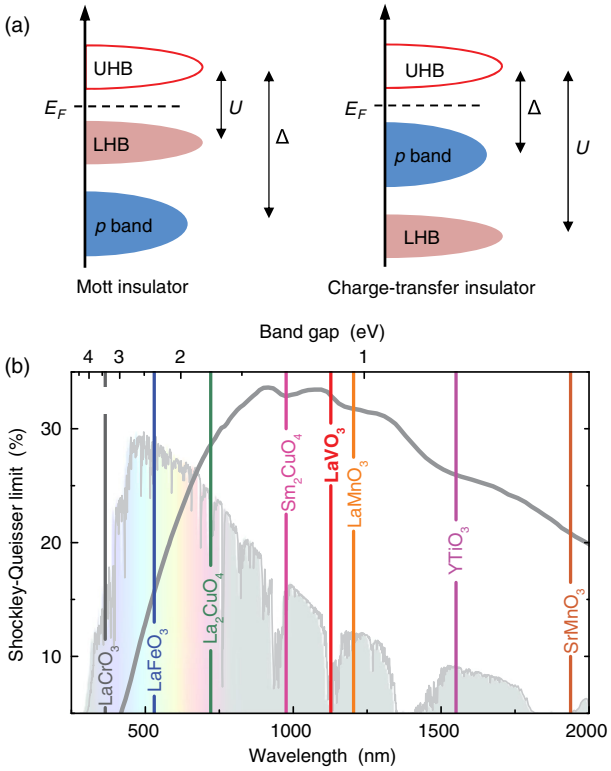

FIG. 1. (a) Schematic illustration of energy levels for the Mott insulator and charge-transfer insulator. (b) Shockley-Queisser limit as a function of band gap, along with the solar spectrum. The band gaps of various prototypical TMOs are marked.

will naturally integrate with other functional TMOs in heterojunction devices and supply power for driving other functionalities. Past work has centered on fabricating photovoltaic devices based on the conventional TMOs [14–18], including cuprates, manganite, and doped $SrTiO_3$.

In this work, we explore perovskite-structured $LaVO_3$ (LVO) as a light absorber in photovoltaic devices, and its optical and transport properties are investigated in detail. With the electron configuration of $3d^2$ ($t_{2g}{}^2$) in the trivalent vanadium cation, LVO is well known as a prototypical Mott insulator [19]. In this strongly correlated electron system, the strong $3d$ electron-electron interaction splits the V t_{2g} band into a fully occupied lower Hubbard band (LHB) and an empty upper Hubbard band (UHB) [10,20]. The optical band gap obtained from the photoconductivity measurement is approximately 1.1 eV [10,11]. According to the Shockley-Queisser limit curve presented in Fig. 1(b) [21] the band gap of LVO is close to the optimal value for solar-energy conversion. Moreover, similar to the well-studied $LaAlO_3/SrTiO_3$ interface, the polar discontinuity at the $LaVO_3/SrTiO_3$ interface is also identified [22], and the resultant internal potential gradient is theoretically suggested to be useful in separating the photon-generated electron-hole pairs [9]. These results strongly imply that the LVO can be a promising candidate as a light absorber in solar cells. Optical absorption and carrier transport behaviors, which are of critical importance for solar-absorbing materials, need to be directly characterized for LVO, and the potential of applying such a Mott insulator in photovoltaic devices also needs to be evaluated. To this end, we fabricate high-quality LVO films and directly characterize their optical absorption and carrier transport properties. To elucidate the band structure of LVO, first-principles calculations are carried out, which reveal the correlation between the fine structures of the absorption spectrum and the excitations between different orbital-derived bands. Furthermore, we make a Mott-insulator-based solar cell and evaluate the performance of such proof-of-concept devices. Overall, our results pave the way for developing a class of photovoltaic devices based on materials with strongly correlated electrons.

II. DETAILS OF EXPERIMENTS AND FIRST-PRINCIPLES CALCULATIONS

A. Thin-film deposition and characterization

Epitaxial LVO films of 120-nm thick are grown by the pulsed-laser-deposition (PLD) method on various substrates including (001)-oriented $(LaAlO_3)_{0.3}(Sr_2AlTaO_6)_{0.7}$ [LSAT(001)], $LaSrAlO_4$ [LSAO(001)], Nb-doped (0.05 wt %) $SrTiO_3$ [NSTO(001)], and quartz. The ceramic $LaVO_4$ target is prepared via the standard solid reaction method. During deposition, the substrate is kept at 700 °C under a high vacuum below 10^{-6} Torr [23,24]. The KrF laser ($\lambda = 248$ nm) energy and repetition rate are set at approximately 2 J/cm^2 and 10 Hz, respectively, resulting in a growth rate of approximately 2 nm/ min. The film thicknesses are measured using a profilometer (Veeco Detak). The structure of the films is characterized by x-ray diffraction (XRD, Panalytical X'pert) using Cu $K\alpha_1$ radiation ($\lambda = 1.5406$ Å), including ω-2θ linear scan and reciprocal-space mapping (RSM). X-ray photoelectron spectroscopy (XPS) measurements are carried out in a custom-built ultra-high-vacuum system with Mg $K\alpha$ (1253.6 eV) as the excitation source. During the measurements, the base pressure is approximately 2×10^{-9} Torr, and the O $1s$ signal is calibrated to 530.2 eV as the binding energy reference. The temperature (T)-dependent magnetization (M), resistivity (ρ), and Hall effects are measured in a superconducting quantum-interference-device magnetometer (MPMS) and physical-property-measurement system (PPMS) from Quantum Design. The absorption spectra are measured using a UV-Vis-NIR spectrophotometer (Agilent Technologies, Cary-6000i) in the transmittance mode.

B. Solar-cell fabrication and characterization

To fully evaluate the potential of LVO in photovoltaic devices, we fabricate solar cells with three different kinds of configurations in this work. The mesoporous-structured devices, which give the best performance, are constructed

on patterned fluorine-doped tin-oxide (FTO)-coated glasses. The device synthesis is similar to the procedure in our previous reports [25,26]. First, a compact TiO_2 (c-TiO_2) blocking layer of roughly 40 nm is deposited by spin coating a solution of 0.15M titanium isopropoxide in ethanol and then baked at 510 °C for 30 min. Next, a mesoporous TiO_2 (m-TiO_2) layer, which contains connected TiO_2 nanoparticles, is deposited by spin coating the TiO_2 paste (Dyesol 18NR-T) diluted in ethanol with mass ratios ranging from 1:1.5 to 1:5 to give various thicknesses. This mesoporous layer is further annealed in air at 540 °C for 1 h. The LVO layer is deposited by the PLD method. The recipes are similar to those used for epitaxial LVO films, except that the substrate temperature is decreased to 600 °C to protect the FTO glass. Then, as the hole transporting material, 2,2′,7,7′-tetrakis-(*N*,*N*-di-*p*-methoxyphenylamine)9,9′-spirobifluorene (sprio-OMeTAD) is spin coated onto the LVO layer and then dried in dark dry air overnight. Finally, a 60-nm Ag electrode is deposited by thermal evaporator. In this device structure, the LVO serves as the light absorber, and the mesoporous TiO_2 and spiro-OMeTAD are employed as the electron and hole transporters, respectively. As the second configuration, the planar junction device without an m-TiO_2 layer is also fabricated on the top of FTO-coated glass. The procedures for depositing the c-TiO_2, LVO, sprio-OMeTAD layers, and the Ag electrodes are the same as those for the mesostructured devices. The thickness of LVO is 50 nm. For fabricating the epitaxial film device, which is the third device configuration, 50-nm LVO film is epitaxially grown on the NSTO(001) substrate. A silver electrode is deposited on the exposed NSTO surface, and 10-nm semitransparent Au electrodes with a mesastructure ($200 \times 200\ \mu m^2$) are deposited on the LVO film surface for light-illuminated measurements.

The cross-section image of the mesoporous-structured cell is obtained using a field emission scanning electron microscope (SEM, FEI Quanta 600FEG). For characterizing the cell performances, simulated air mass 1.5 (AM1.5) sunlight with power intensity of 100 mW cm^{-2} is generated by a Newport Oriel Sol 3A solar simulator. The current density-voltage (J-V) curves are recorded with a source-meter (Keithley 2400).

C. First-principles calculations

The band structure and density-of-states (DOS) calculations are performed using first principles within the framework of density-functional theory (DFT) via the Vienna *Ab Initio* Simulation Package code with the projector-augmented-wave potentials for electronic interaction and the Perdew-Bruke-Ernzerhof functional for electron exchange and correlation [27–29]. The polarized optical absorption spectra are calculated from the dielectric function. We construct a ten-atom $\sqrt{2} \times \sqrt{2} \times 1$ supercell ($a = b \cong \sqrt{2}c$) in order to take into account the C-type antiferromagnetic spin order [9]. The on-site Coulomb repulsion U for the d electrons of the V element is taken into account as a result of the strong correlation effect. We carry out the calculations with different U values and find that $U = 3.6$ eV leads to the best match between the calculated polarized absorption and the experimental optical absorption spectrum. In the calculations, all the atoms are allowed to relax until the Hellmann-Feynman forces acting on them become less than 0.01 eV/Å. The final lattice parameters we obtain are $a = b = 5.513$ Å, $c = 4.009$ Å, which are close to the values from previous experiments and first-principles calculations [9,24].

III. RESULTS AND DISCUSSION

A. Epitaxial quality and oxygen stoichiometry

Figure 2(a) shows the XRD ω-2θ linear scan measured from the LVO/LSAT(001) film with a thickness of 120 nm. For the film deposited at high vacuum below 10^{-6} Torr, the spectrum shows only the LSAT(00l) and LVO(00l) peaks (in the pseudocubic notation) over the whole scanning range, demonstrating that the film is single-phase perovskite-structured LVO. In contrast, for the film deposited at 10^{-3} Torr, diffraction peaks related to monoclinic $LaVO_4$ appear instead of the LVO(00l) peaks, which implies that

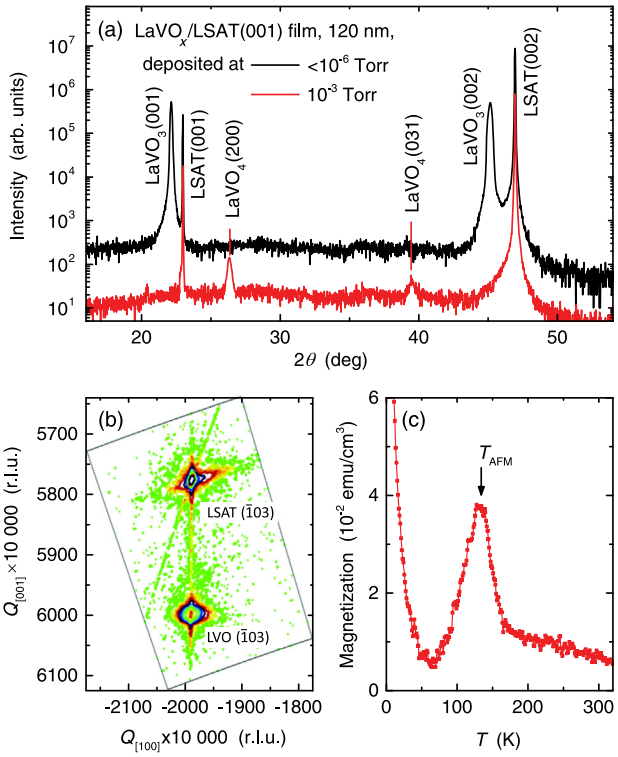

FIG. 2. (a) XRD 2θ-ω scan of the $LaVO_x$ films grown on LSAT (001) substrates with different oxygen pressures. (b) RSM data collected around the LSAT and LVO $(\bar{1}03)$ reflections. (c) The M-T curve measures at 100 Oe. The antiferromagnetic temperature T_{AFM} is marked by the solid arrow.

the high-vacuum condition is indispensable for growing high-quality LVO films [23]. The strain state of the epitaxial LVO film is further characterized via RSM measurements. As shown in Fig. 2(b), the sharp and concentrated reflection from the LVO film shares the same in-plane lattice constant as that of the substrate, implying a coherent growth and fully strained state of the LVO film [30–32]. The out-of-plane pseudocubic c-axis constant calculated from the RSM data is 4.01Å, which is consistent with the one calculated from the ω-2θ linear scan. The bulk lattice parameter of LVO in the pseudocubic notation is approximately 3.925 Å, while the cubic LSAT substrate has a lattice parameter of 3.868 Å. The resultant lattice mismatch of 1.45% gives rise to the compressive strain and elongates the out-of-plane b axis of LVO.

The field-cooling M-T curve measured at 100 Oe is shown in Fig. 2(c). The observed peak at approximately 135 K (T_{AFM}) signifies the paramagnetic-antiferromagnetic transition associated with the orbital-ordering state [19]. The T_{AFM}, which is close to that reported for bulk $LaVO_3$ (143 K), also confirms the dominated V^{3+} valence state since the antiferromagnetic transition in LVO_4 appears at a much lower temperature [33]. We also note here that the high-vacuum-growth condition may not only stabilize the LVO_3 phase and prevent the V^{5+} valence state but also reduce some V^{3+} ions into V^{2+} ones and produce oxygen vacancies (V_{O}) [34,35]. The oxygen-related defects may disturb the formation of long-range antiferromagnetic order and slightly lower the antiferromagnetic transition.

The XPS technique is employed to further analyze the valence state of V cations. The high-resolution spectra around the O 1s and V 2p peaks are measured on the films deposited at pressures of 10^{-3} and 10^{-6} Torr. For the film deposited at 10^{-3} Torr, as shown in Fig. 3(a), the V 2p XPS signal can be fitted by the V^{5+} and V^{4+} components [36]. In contrast, for the film deposited below 10^{-6} Torr, the V^{3+} state contributes as the main component to the V 2p signal, demonstrating that the high-vacuum-growth condition can stabilize the LVO phase. In addition, the spectrum also shows a weak component at lower binding energy, which can be assigned to the V^{2+} state. The appearance of this low valence state also implies that the V_{O} are introduced in the LVO sample during the film growth. By calculating the integrated areas of V $2p_{3/2}$ peaks related to V^{3+} and V^{2+} valence states, the percentage of V^{2+} in the oxygen-deficient $LaVO_{3-\delta}$ film can be roughly estimated as approximately 2.4%. According to the constraint of charge neutrality, the oxygen nonstoichiometry δ is estimated as 0.012 corresponding to a V_{O} concentration of 2×10^{20} cm^{-3}.

We should note that multivalence of transition-metal ions in TMO is a unique advantage for band-gap tuning, important for tailoring their optical and transport properties. Particularly, perovskite LVO samples appear black,

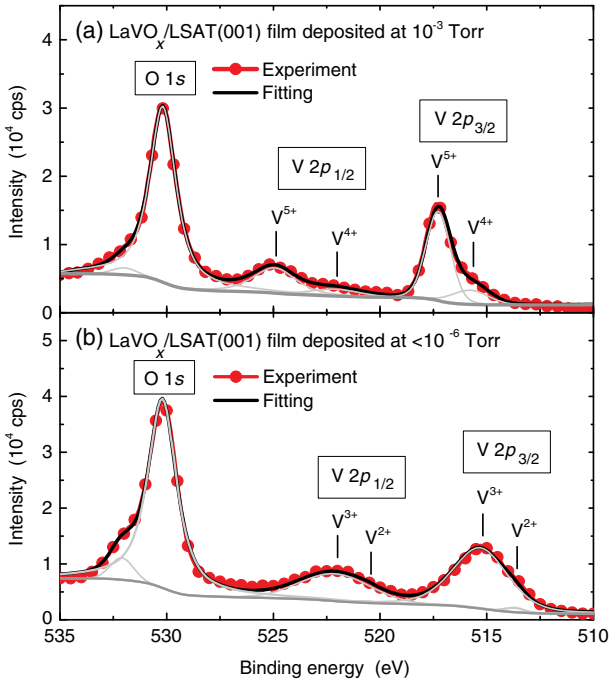

FIG. 3. XPS spectra and fitting curves of the LVO films deposited at (a) 10^{-3} Torr and below 10^{-6} Torr. The various valence states of vanadium cation are labeled.

indicating strong light absorption in the visible range, whereas monoclinic $LaVO_4$ is transparent with little light absorption. At the same time, the multivalence nature of TMOs like LVO also implies that they can accommodate high-density defects while maintaining the charge neutrality posing as a tremendous challenge in the synthesis of samples with high purity; these defects will scatter and trap photocarriers, reducing their transport mobility and compromising the device efficiency.

B. Optical absorption and band structure

Absorption spectra of the LVO films at room temperature are systematically measured and analyzed. As shown in Fig. 4(a), the photon-energy (E)-dependent absorption coefficient (α) curve exhibits an absorption onset at approximately 1 eV and then two subsequent peaks at 1.75 and 2.39 eV. These two peaks overlap well with the solar spectrum in the visible range, and the maximum value of α at 519 nm is close to 10^5 cm^{-1}. After a slight decrease at approximately 3 eV, the absorption increases again in the UV range. The absorption spectrum of LVO can be well fitted by five broadened Gaussian peaks [37,38], and the peak positions are summarized in Table I. As shown in the inset of Fig. 4(a), the absorption of LVO is significantly higher than that of crystalline silicon (c-Si) in the visible range and even compares favorably with CdTe and amorphous silicon (a-Si) at long wavelengths, indicating that LVO is promising for harvesting solar light. We also grow LVO films on quartz and LSAO(001) substrates, yielding

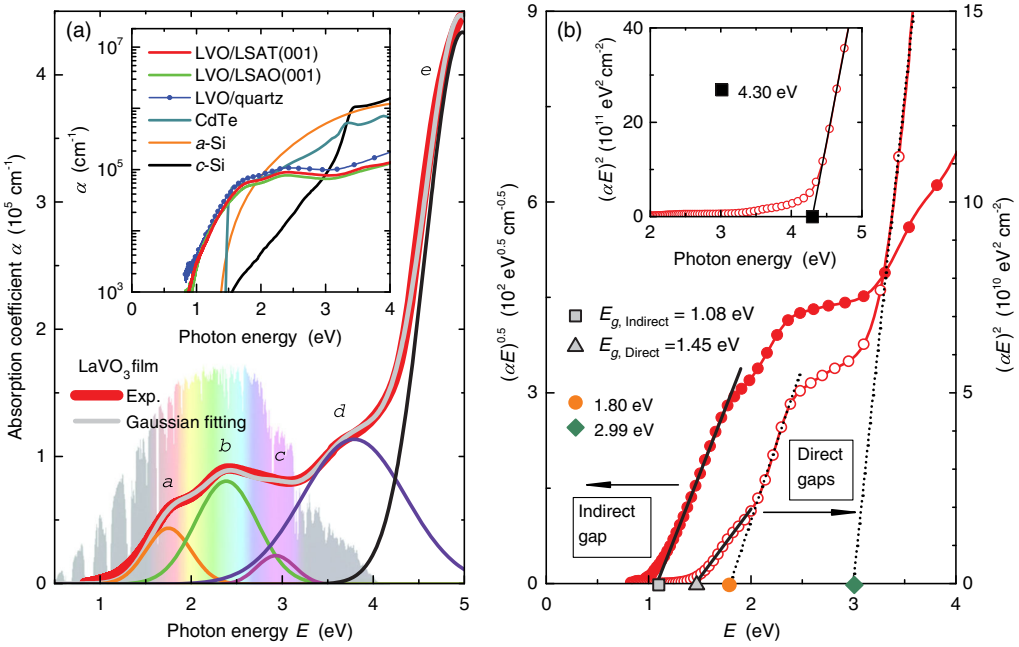

FIG. 4. (a) Experimental absorption spectrum measured from the LVO/LSAT(001) film and fitting curves with five Gaussian peaks labeled a to e. The inset shows the energy-dependent absorption coefficient data of LVO films grown on LSAT(001), LSAO (001), and quartz substrate, in comparison with those of c-Si, α-Si, and CdTe. (b) $(\alpha E)^2$ and $(\alpha E)^{1/2}$ versus E plots for analyzing the band gap of LVO. The solid (dashed) straight lines mark the indirect (direct) band edges. The inset shows the direct band gap analysis in the higher-energy range.

polycrystalline and epitaxial films with larger compressive strain, respectively. Their absorption spectra [inset of Fig. 4(a)] are similar to that of the LVO/LSAT(001) film, implying that the strain state does not play a significant role in determining the optical properties of LVO.

Figure 4(b) shows the Tauc plots of $(\alpha E)^2$ and $(\alpha E)^{1/2}$ versus E, which are used to determine the nature and size of the band gap [39,40]. The $(\alpha E)^{1/2}$ versus E plot displays a sharp and linear rise above the absorption edge, and the linear extrapolation of this curve to zero yields an indirect gap of 1.08 eV. This value is close to the optical gap of 1.1 eV obtained in previously reported photoconductivity measurements [10,11]. In contrast, the $(\alpha E)^2$ versus E plot shows a more complex behavior. The linear fitting at the absorption edge gives a larger direct gap of 1.45 eV but exhibits a large fitting error. In the higher-energy range, a set of direct band gaps at 1.80, 2.99, and 4.30 eV can be clearly identified, revealing a hierarchical band-gap behavior [41]. These data suggest that LVO has a fundamental indirect energy gap, which is in line with the gradual enhancement at the absorption edge. Furthermore, the hierarchal direct gaps at higher energies indicate that the strong electron correlation in LVO may enable not only an indirect transition from the LHB to UHB, but also several interband and intraband excitations, leading to the wide-range absorption of LVO.

To further understand the optical absorption behavior and its correlation with the band structure of LVO, we perform the first-principles calculations within the framework of DFT. In Figs. 5(a) and 5(b), the band structure and the DOS of LVO are presented. The band structure, indeed, shows an indirect band gap between the valence-band maximum (VBM) at X_1 and the conduction-band minimum (CBM) at Γ_3. The DOS clearly shows that the band gap is located between the UHB and LHB of the V t_{2g} band, and the V e_g band and O $2p$ band are located at higher and lower energies, respectively, coinciding with the band structure revealed by the high-energy photoconductivity and ultraviolet photoelectron spectroscopy measurements [10,20]. Moreover, from the energy—wave-vector (E-k)

TABLE I. Summary of absorption peak positions and band gaps derived from the experimental absorption spectrum and the first-principles calculation results. The possible transitions that may contribute to these absorption peaks are also proposed.

	Absorption peaks			Band gaps			
	Gaussian	GGA + U	Assignment	Optical gaps		Calculated band gaps	
				(Forbidden)		$X_1 \rightarrow \Gamma_3$	0.51 eV
(a)	1.75 eV	1.78 eV	V $t_{2g} \rightarrow$ V t_{2g}	Indirect	1.08 eV	$X_1 \rightarrow \Gamma_4$	1.13 eV
(b)	2.39 eV	2.37 eV	V $t_{2g} \rightarrow$ V t_{2g}	Direct	1.80 eV	$\Gamma_2 \rightarrow \Gamma_3$	1.68 eV
(c)	2.95 eV	3.02 eV	O $2p \rightarrow$ V t_{2g}	Direct	2.99 eV	$\Gamma_1 \rightarrow \Gamma_4$	3.05 eV
(d)	3.75 eV	3.67 eV	O $2p \rightarrow$ V t_{2g}				
(e)	4.99 eV	5.13 eV	O $2p \rightarrow$ V e_g	Direct	4.30 eV	$\Gamma_1 \rightarrow \Gamma_5$	4.04 ± 0.31 eV

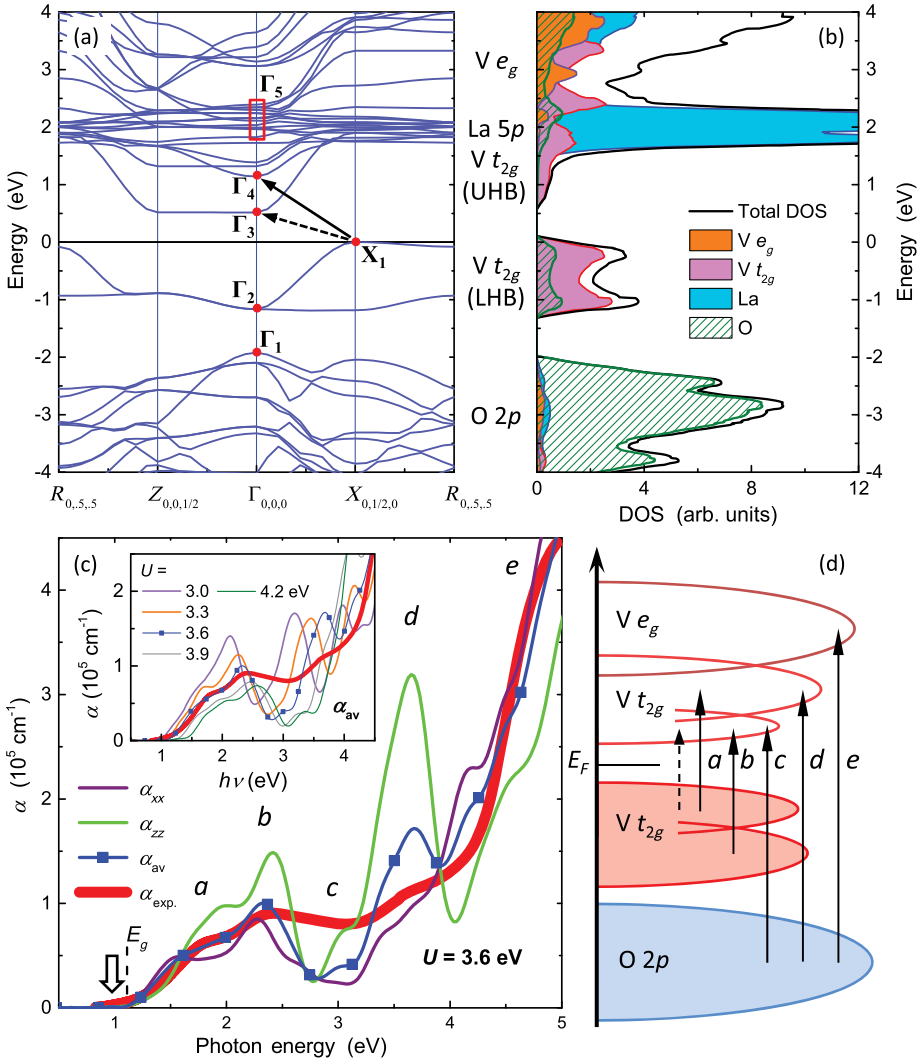

FIG. 5. (a) Band structure of LVO calculated using the GGA + U method. Some important k positions, Γ_1 to Γ_4 and X_1, are marked. (b) Calculated total DOS along with the partial contributions from O 2p, V 3d (including the V t_{2g} and V e_g) and La 5p bands. (c) Calculated curves of absorption coefficient α_{xx}, α_{zz}, and α_{av}, in comparison with the experimental spectrum. The indirect band gap of 1.1 eV is marked by a dashed line, and the absorption tail below the band-gap energy is highlighted by an arrow. The inset shows the α_{av}-E curves calculated with various U values. (d) Schematic band diagram of LVO. The proposed optical transitions (solid arrows) that may contribute to the light absorption are labeled a to e, and the possible forbidden transition (dashed arrow) is also shown.

dispersion and DOS curves, some fine structures can be discerned in the V t_{2g}, V e_g, and O 2p bands. In Fig. 5(a), we mark some positions in the E-k plot which may contribute to the optical transitions.

Notably, the indirect energy gap between X_1 and Γ_3 is 0.51 eV, much smaller than the optical gap (1.08 eV) determined from the absorption spectrum. Here, we note that a larger fundamental band gap can be obtained by choosing a larger U value in the calculation. However, for a fundamental band gap of 1.0 eV, the required U is up to 4.2 eV, which is much higher than that given in previously reported experimental and theoretical works [9,20]. Furthermore, the calculated absorption spectrum using such high U values shows substantial deviation from the experimental one. Therefore, the smaller fundamental band gap should be the intrinsic property of LVO rather than the consequence of an improper U value. We propose two possible scenarios to explain the derivation between the optical band gap and the fundamental band gap. One scenario is related to the dipole-transition nature of light absorption. Since the LVO crystal structure has an inversion center, the electric-dipole operator with odd parity can enable only optical transitions between states with opposite parities [42,43]. Accordingly, if the Γ_3 and Γ_4 points have different parities, the band-edge transition from X_1 to Γ_3 could be forbidden, while the $X_1 \rightarrow \Gamma_4$ with energy of 1.13 eV is allowed, resulting in the indirect gap around 1.1 eV, in line with the value derived from the optical absorption spectrum. In the other possible scenario, even if the $X_1 \rightarrow \Gamma_4$ transition might not be strictly dipole forbidden due to the lattice distortion, the low DOS near the CBM edge could significantly suppress the optical absorption across the UHB and LHB. This scenario is consistent with the calculated result shown in Fig. 5(b), where the DOS near the CBM is much lower than that near the VBM.

As summarized in Table I, in addition to the indirect transition $X_1 \rightarrow \Gamma_4$, the energies of the direct transitions $\Gamma_2 \rightarrow \Gamma_3$ (1.68 eV) and $\Gamma_1 \rightarrow \Gamma_4$ (3.05 eV) are close to the hierarchal direct gaps of 1.80 and 2.99 eV obtained from the $(\alpha E)^2$-E linear extrapolations. The $\Gamma_1 \rightarrow \Gamma_5$ transition in

the energy range of 4.04 ± 0.31 eV, despite being hidden inside the strongly intermixed V e_g, V t_{2g}, and La $5p$ bands, roughly matches the observed direct gap of 4.30 eV.

Figure 5(c) presents the calculated polarized optical absorption curves (α_{xx} and α_{zz}). For the absorption measurements in the transmittance mode, although the incident light is parallel to the c axis of the single-crystal LVO film, it can be scattered by structural defects, surface roughness, and atomic steps on the substrate [9]. Considering this factor, we plot not only α_{zz} but also α_{xx} and calculate $\alpha_{\mathrm{av}} = (2\alpha_{xx} + \alpha_{zz})/3$. Moreover, we calculate the polarized optical absorption curves with U varying from 3.0 to 4.2 eV, which should well cover the possible U values reported in the literature [9,20]. As shown in the inset of Fig. 5(c), the α_{av}-E curves show a blueshift with increasing U due to the larger Mott-Hubbard band gap, and the curve with $U = 3.6$ eV, indeed, gives rise to the best match with the experimental absorption spectrum. Characteristic features of the α_{av}-E curve include peaks at 1.78 and 2.37 eV in the visible range, a weak peak at 3.02 eV, and two strong absorption peaks at 3.67 and 5.13 eV in the UV range. The peak positions, as summarized in Table I, are close to those of the Gaussian peaks derived from fitting to the experimental spectrum. We should note that in the DFT + U framework, the electron-hole correlation effect is not included. According to the report with the Bethe-Salpeter equation approach [44], the electron-hole interaction can induce a redshift of the optical spectrum. Therefore, the U value in our case might be slightly underestimated. Nevertheless, we believe that our DFT + U calculations can quantitatively predict the band structure and the absorption spectrum of LVO.

In Fig. 5(d), the schematic band diagram of LVO and the possible associated optical transitions are proposed. The UHB and LHB of the V t_{2g} band are treated as two subbands with some hybridization, taking into account the fine structures shown in Figs. 5(a) and 5(b). We can assign the low-energy absorption peaks a and b to the two d-d transitions between the lower and higher subbands, in accordance with the indirect and direct gaps at 1.08 and 1.80 eV, respectively. In the higher-energy range, the p-d excitations from the O $2p$ band to the V t_{2g} band contribute to the absorption peaks c and d, as well as the direct gap at 2.99 eV. The peak e can be assigned to the p-d excitations from the O $2p$ band to the V e_g band. For the d-d transition-related absorption peaks a and b, the experimental and calculated curves exhibit close intensities and similar line shapes, while the p-d transition-related peaks c, d, and e in the experimental spectrum are broader and weaker than the calculated peaks. Considering the fact that the high-vacuum-deposition process could introduce oxygen nonstoichiometry in the LVO films, the O $2p$ band structure may deviate from the ideal case, thus, weakening the p-d transition-related light absorption. In addition, as marked by the open arrow in Fig. 5(c), the experimental spectrum shows a gradual absorption tail below the band gap of 1.1 eV, while the calculated α_{av}-E curve exhibits a much sharper absorption edge. This behavior implies that the oxygen-related defects may form band-tail states below the CBM, and the optical transitions between these in-gap states and the VBM could contribute to the optical absorption below the band gap [45].

We should note here, however, that the complex behavior of hierarchical gaps in LVO clearly warrants further investigation, and more work is needed to unambiguously assign the features of the light-absorption data to the calculated energetic transitions between the subbands of LVO. Nevertheless, the insights achieved from the first-principles calculations will guide the experimental efforts on fine-tuning the optical absorption properties of such strongly correlated electron systems.

C. Charge transport properties of LVO

To characterize the carrier transport of LVO, ρ-T and Hall measurements are carried out. As shown in Fig. 6(a), the ρ-T curve of the LVO film shows a semiconducting behavior in the whole temperature range. At temperatures above T_{AFM}, the ρ-T curve follows the mechanism of thermally activated polaron hopping (TAP):$\rho \propto T\exp(E_a/k_BT)$, where k_B is the Boltzmann constant, and E_a is the activation energy [46]. As shown in the top inset of Fig. 6(a), the linear fitting of the $\ln(\rho/T)$ vs the

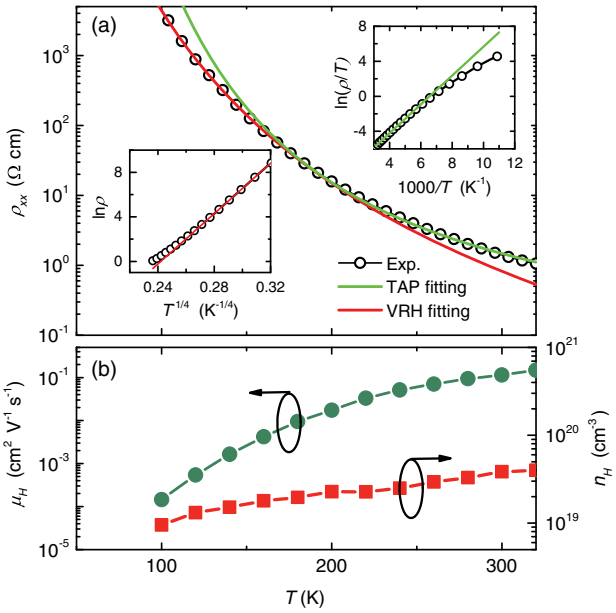

FIG. 6. (a) ρ-T curve (open circles) measured from the LVO/LSAT(001) film along with the TAP and VRH fitting curves (solid lines). The top and lower inset show the $\ln(\rho/T)$ vs $1000/T$ and $\ln\rho$ vs $T^{-1/4}$ dependence, respectively, as well as the corresponding linear fitting curves. (b) Temperature-dependent carrier mobility and concentration data extracted from the Hall measurements.

$1000/T$ plot gives rise to E_a of 0.14 eV, which is much smaller than the optical band gap of 1.1 eV. This small activation energy could be attributed to the excitations from the localized states arising from oxygen-related defects to the conduction band [47]. Below T_{AFM}, the ρ-T behavior appears to follow the three-dimensional variable-range-hopping (VRH) conduction mechanism with $\rho \propto \exp(T_0/T) - 1/4$, as confirmed by the linear dependence of $\ln\rho$ on $1/T^{1/4}$ [lower inset of Fig. 6(a)] [47,48]. This conduction mechanism could originate from the strong carrier localization in the charge-orbital-ordering state below T_{AFM} [48].

Hall measurements are carried out on LVO films in the temperature range of 320 to 10 K, and the extracted carrier concentration and Hall mobility are presented in Fig. 6(b). However, due to the strong carrier localization and high noises, we cannot obtain reliable data below 100 K. The majority carriers are found to be electrons, which is consistent with the previously reported Hall measurements on bulk LVO [19]. The carrier concentration deduced from the Hall coefficient n_H decreases slowly during cooling. n_H at 300 K is measured as 3.85×10^{19} cm^{-3}, comparable with other typical Mott insulators like La_2CuO_4 [49,50]. As the temperature decreases to 100 K, the Hall mobility μ_H quickly decreases from 0.11 cm^2 V^{-1} s^{-1} to 1.46×10^{-4} cm^2 V^{-1} s^{-1}, which could be attributed to the low-temperature carrier localization caused by orbital ordering [19].

The room-temperature electron mobility of LVO (0.11 cm^2 V^{-1} s^{-1}) is much lower than those of conventional solar-cell-grade inorganic semiconductors like Si (approximately 10^3 cm^2 V^{-1} s^{-1}), GaAs (approximately 5×10^3 cm^2 V^{-1} s^{-1}), and $Cu(In, Ga)Se_2$ (CIGS, 90–900 cm^2 V^{-1} s^{-1}) [51,52] but comparable or higher than those of organic semiconductors like [6,6]-phenyl C61-butyric acid methyl ester (2×10^{-3} cm^2 V^{-1} s^{-1}) [53]. Furthermore, the carrier density of LVO without light illumination is substantially higher than that of Si (approximately 10^{16} cm^{-3}), GaAs (10^{17}–10^{18} cm^{-3}), and CIGS (approximately 10^{16} cm^{-3}) [51,52]. V_{O} induced during the film deposition could be the main source of this extrinsic n-type doping and high carrier density. However, the observed value of n_H (3.85×10^{19} cm^{-3}) is 1 order of magnitude lower than the nominal carrier concentration donated by V_{O} in LVO (approximately 4×10^{20}), if we assume that each oxygen vacancy donates two electrons to the conduction band. This discrepancy, which has been observed in other oxygen-deficient TMO systems like $SrTiO_3$ [54], can be explained by the formation of mixed polarons [55,56]. The electrons introduced by intentional doping or unintentional defects in TMO could form polarons due to the strong electron-phonon interaction. Large polarons have wave functions spreading over several lattice sites and contribute free carriers to the transport, whereas small polarons form highly localized in-gap states and trap carriers, thus, leading to the difference between n_H and the nominal carrier concentration. The small $E_a = 0.14$ eV obtained from the TAP fitting implies that the transport is dominated by small polarons which induce the shallow trap states located near the CBM.

Our data analysis suggests that the dominating factor that hinders the carrier transport of LVO should be the polaronic behavior associated with the high-density V_{O}. The resultant shallow traps increase the effective mass of electrons and reduce the carrier mobility. Furthermore, in the LVO-based solar cells, the photoexcited carriers can relax into the self-trapped polaron states [57,58], which increases the recombination rate and shortens the diffusion length of photocarriers in LVO. Therefore, choosing a suitable device design that can not only utilize the strong optical absorption but also rectify the poor carrier transport should be the central challenge for fabricating effective TMO-based solar cells.

The high-density defects may act as trapping centers and give rise to the polaron-type transport, which may hinder the electron-hole-pair separation and reduce the diffusion lengths of photocarriers in solar cells. Hence, choosing a suitable device design that can not only utilize the strong optical absorption but also compensate the poor carrier transport should be the central challenge for fabricating effective LVO-based solar cells.

D. Design and characterization of LVO-based solar cells

Since the optical absorption of LVO matches well with the solar spectrum, we attempt to fabricate and characterize LVO-based solar cells. There are several configurations of solar cells developed for achieving optimum efficiencies using various material systems. In the conventional bulk- and thin-film solar cells, semiconductors are incorporated into planar p-n or p-i-n junctions, serving for both light harvesting and photocarrier transport [59,60]. When applying this configuration into the TMO-based photovoltaic devices, the oxide films can be deposited on n-type silicon or Nb-doped $SrTiO_3$ single-crystal substrates to form p-n junctions, n^+-n junctions, or Schottky diodes [12–16]. However, as we discussed in the section above, the charge transport properties of most TMOs at room temperature are far inferior compared to those of crystalline semiconductors like Si and GaAs. As a result, the optimized thicknesses of a TMO layer in these photovoltaic diodes should be comparable to the depletion layer thickness, which is often only several tens of nanometers due to the high dielectric constant and the associated strong screening effect [61]. If the TMO layer is too thick, there will be no driving force to separate the photocarriers, and no photocurrent will be able to reach the electrodes.

We test first two planar configurations for LVO-based solar cells. In the first type with top-light illumination, semitransparent Au electrodes are deposited on top of the

LVO/NSTO(001) film. A Schottky diode is expected to form at the interface between the Au and the epitaxial film. In the second type with bottom-light illumination, an *n*-type *c*-TiO_2 layer, a LVO polycrystalline film, *p*-type spiro-OMeTAD hole transporter, and Ag electrodes are successively deposited on FTO-coated glass, resulting in a *p*-*i*-*n* junction. The thickness of the LVO layers in both devices is 40 nm. Figures 7(a) and 7(b) present, respectively, the *J*-*V* curves of the two devices measured in dark and under simulated AM1.5, 100-mW cm^{-2} illumination. Both devices show diode-type rectification but negligible photovoltaic effect under light illumination. The observed current rectification in these two devices confirms the existence of a built-in electric field for separating the photoexcited electron-hole pairs in the LVO layer. However, in these planar junction devices, the carrier diffusion length of LVO is much shorter than the film thickness as a result of strong defect-induced trapping; thus, most of the photocarriers will not be able to reach the active interfaces and be collected by electrodes, leading to the poor photovoltaic performance.

To overcome the limitation of the poor carrier transport property of LVO, we incorporate additional electron-transport material (ETM) and hole-transport material (HTM) into a structure similar to the design of dye-sensitized solar cells (DSSCs). In this solar-cell structure, a huge number of internal interfaces between the individual solar absorber and nanostructured charge transport media enable the separation and collection of photon-excited electron-hole pairs [62]. The independent transportation routes for electrons and holes reduce the recombination rate and lower the demand on the carrier transport ability of light-absorbing LVO. The typical light absorbers in solid-state DSSCs include metal complexes and organic dyes [63], inorganic semiconductors [64], quantum dots [65], and organometal halide perovskites [66]. We employ LVO as an inorganic light absorber to construct Mott insulator solar cells.

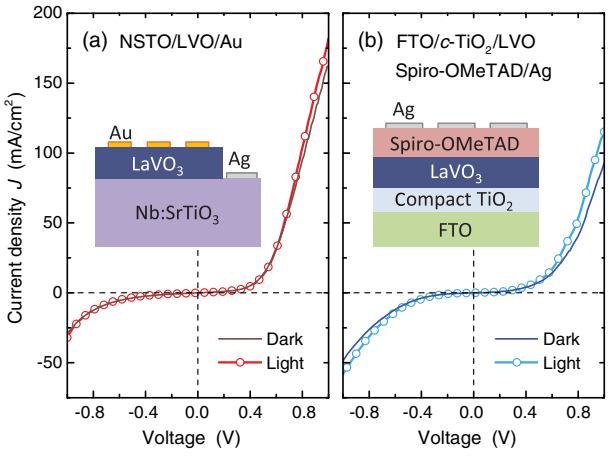

FIG. 7. Dark and illuminated *J*-*V* curves of (a) the device with semitransparent Au electrodes deposited on the LVO/NSTO(001) film and (b) the DSSC-like *c*-TiO_2/LVO/spiro-OMeTAD device.

To construct the device, a compact and then a mesoporous layer of *n*-type TiO_2 are prepared on FTO-coated glass, and they serve as a transparent ETM. Right on the *m*-TiO_2 layer, LVO is deposited using the PLD method, followed by the spin-coated spiro-OMeTAD as the HTM. The cross-sectional SEM image of a representative device is shown in Fig. 8(a). The *m*-TiO_2 film, together with the LVO layer, has a thickness of approximately 550 nm, and the spiro-OMeTAD forms a capping layer of approximately 100 nm on the LVO *m*-TiO_2 layer. Because of the large lattice mismatch between LVO and TiO_2 as well as the random orientations of TiO_2 nanoparticles, the LVO layer is polycrystalline, but its optical absorption properties are similar to that of epitaxial LVO films, as we discussed previously.

In most DSSCs, the light-absorbing dyes are synthesized via solution processes, and they can conformably coat the pores of *m*-TiO_2. In this work, we use the vapor-phase PLD method to prepare the LVO, which is not effective to penetrate deeply into the *m*-TiO_2 structure. To clarify this issue, energy-dispersive x-ray spectroscopy (EDX) is used to investigate the elemental distribution in the heterojunction. As shown in the elemental line scan in Fig. 8(b), the profiles of Ag $L\alpha$, Sn $L\alpha$, and Ti $K\alpha$ change sharply at the interfaces between the different layers. By contrast, the V $K\alpha$ profile shows a strong intensity at the interface between spiro-OMeTAD and TiO_2, and then the intensity decreases gradually as the probe goes deeper into the *m*-TiO_2 layer. These data indicate that most LVO is accumulated within the top 200 nm of the mesoporous structure. Based on the SEM and EDX analysis, the schematic device architecture is presented in Fig. 8(c). During the high-vacuum PLD deposition process, the ions and clusters inside the laser-ablated plume move ballistically and get deposited onto the *m*-TiO_2 layer; hence, only the TiO_2 nanoparticles in the top portion of the film are coated by LVO. Even so, the mesoporous structure helps increase the TiO_2/LVO interface area, leading to a more efficient electron extraction compared to the planar junction devices. Unlike the LVO layer, solution-processed HTM spiro-OMeTAD completely fills the pores of the *m*-TiO_2 layer, which ensures the efficient hole collection at the anode.

We should note here that a suitable solution-based synthesis route for preparing high-quality LVO is still not available. In a previously reported experiment [67], $LaVO_4$ was synthesized via the sol-gel process, while LVO can be obtained only by reducing the $LaVO_4$ via heating with Zr metal at 850 °C in vacuum. This method can be used in synthesizing LVO powders and polycrystalline pellets, but in the solar-cell fabrication, the high-temperature reduction process will easily destroy the FTO-coated glass as well as the TiO_2 layer. Accordingly, in this work, we consistently use the PLD method to prepare the LVO layers in fabricating solar cells.

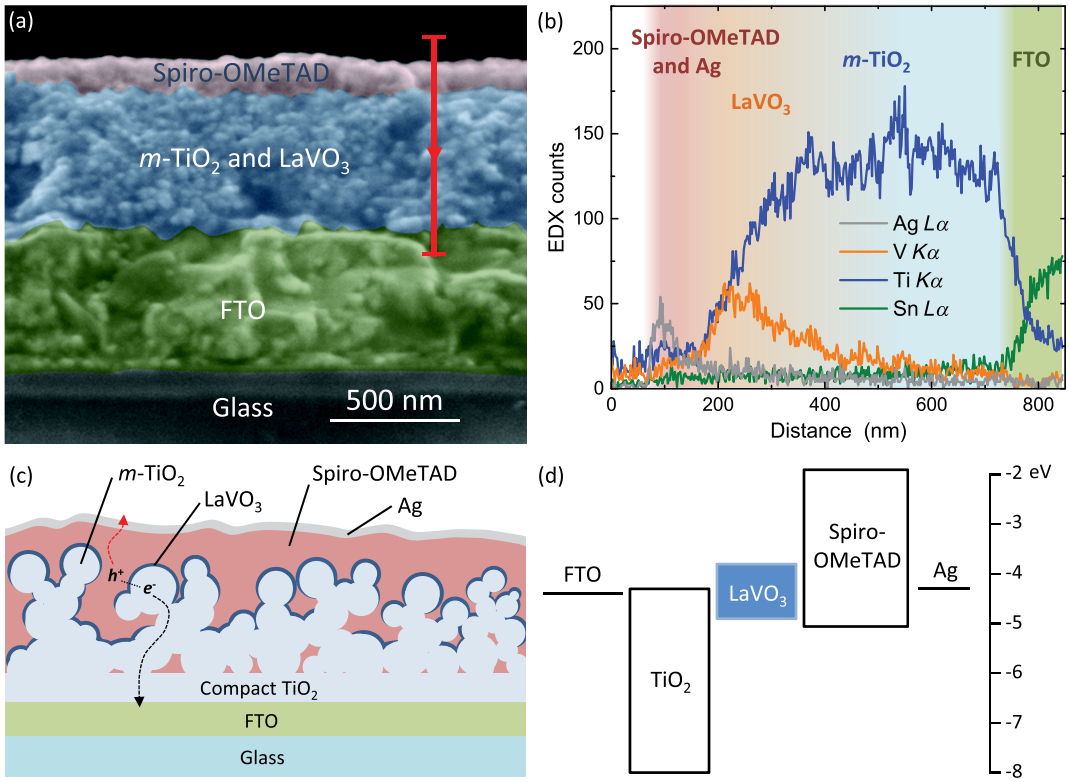

FIG. 8. (a) Cross-sectional SEM image of the m-TiO_2/LVO/spiro-OMeTAD heterojunction solar cell. (b) EDX elemental line scan profiles along the red line marked in (a). (c) Schematic of the device architecture. Note that the LVO layer (deep blue) covers only the top surfaces of m-TiO_2. (d) Energy levels of the various components in the solar cell.

Figure 8(d) shows the energy-level diagram of the LVO solar cell. The LVO has a work function of approximately 4.3 eV [10]; thus, its CBM and VBM should be 3.7 and 4.9 eV, respectively, if we consider LVO as an insulator with the Fermi level being located roughly at the middle of the band gap. Accordingly, TiO_2 exhibits a good band alignment with LVO for collecting electrons and blocking holes. For spiro-OMeTAD, the lowest unoccupied molecular orbital is much higher than the VBM of LVO, ensuring the blockage of electrons. The highest occupied molecular orbital energy level of spiro-OMeTAD (5.11 eV), despite being slightly lower than the VBM of LVO, is higher than most of the widely used polymeric HTM [68], which can minimize the energy barrier at the absorber-HTM interface and assist the hole collection.

The J-V curves measured from the best-performing m-TiO_2/LVO/spiro-OMeTAD solar cell are shown in Fig. 9(a). The dark J-V curve appears as a rectifying diode, and the curve under simulated AM1.5, 100-mW cm^{-2} illumination shows a short-circuit photocurrent (J_{SC}) of 0.78 mA/cm^2, an open-circuit voltage (V_{OC}) of 0.40 V, and a fill factor (FF) of 39%, yielding an overall power conversion efficiency (PCE) of 0.12%. As shown in Fig. 9(b), the J-V curve measured on the m-TiO_2/spiro-OMeTAD device without the LVO absorber shows also good rectifying behavior but a significantly reduced photocurrent and PCE, which confirms that in the m-TiO_2/LVO/spiro-OMeTAD heterostructured solar cells, LVO, indeed, acts as an absorber to produce electron-hole pairs and contributes to the photovoltaic effect. Moreover, compared with the planar junction devices [Fig. 7(b)], both the photovoltaic effect and the current

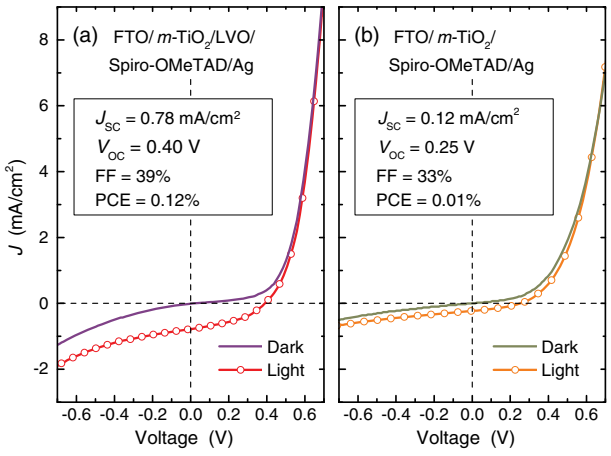

FIG. 9. Dark and illuminated J-V curves of (a) m-TiO_2/LVO/spiro-OMeTAD heterojunction solar cell and (b) m-TiO_2/spiro-OMeTAD diode without LVO. J_{SC}, V_{OC} FF, and PCE of these devices are also given.

rectification of the mesostructured device are significantly improved, indicating the mesoporous-structured ETM facilitates constructing efficient LVO-based solar cells. This m-TiO_2 layer may not only provide efficient collection of photon-generated electrons, but it will also help spiro-OMeTAD to form a uniform and continuous film, giving rise to a better performance of the mesostructured diode.

To further clarify the effects of the m-TiO_2 layer and LVO absorber on the device performance, a series of devices with various thicknesses of m-TiO_2 (t_m) and LVO (t_L) are fabricated and characterized. Note that the precise thickness of the LVO layer deposited on m-TiO_2 is difficult to determine because of the large surface roughness of the porous structure. t_L is actually the equivalent thickness measured from LVO films deposited on flat quartz substrates with the same deposition conditions. Because of the large surface area of the m-TiO_2 layer, the actual average thickness of the LVO layer should be much smaller but in proportion to t_L. Nevertheless, the observed trend of the solar-cell performance on t_L still reflects the dependence on the exact thicknesses of the LVO layers. The J-V curves of the cells with various t_L (t_m) are shown in Fig. 10(a) [Fig. 10(b)], and the V_{OC} and J_{SC} extracted from the J-V curves are summarized in Figs. 10(c) and 10(e) [Figs. 10(d) and 10(f)]. As t_L increases, the V_{OC} exhibits a monotonic decrease from 0.48 V at $t_L = 40$ nm to 0.32 V at $t_L = 200$ nm. A similar trend of absorber thickness dependence of V_{OC} is observed in DSSC [69]. On the one hand, the average optical power density within the LVO decreases as the t_L increases, which reduces the photon-generated carrier density. On the other hand, when the absorber becomes thicker, the carriers generated within the absorber have more chances of recombining before being extracted by the ETM and HTM. Since the V_{OC} in DSSC is highly dependent on the photon-generated carrier density at the cathode and anode [70], both effects can result in the reduction of V_{OC}. Considering the high density of trapping states in the LVO layer, the charge recombination scenario could be the dominant origin for the t_L dependence of V_{OC}. The J_{SC}, with increasing t_L, shows a nonmonotonic change with the maximum value occurring at $t_L = 120$ nm. As the t_L increases from 40 to 120 nm, the stronger light absorption increases the total number of photon-generated carriers and, hence, enhances the J_{SC}. However, similar to the behavior of t_L-dependent V_{OC}, further increasing the t_L up to 160 nm increases the trap-assisted recombination, leading to a less-effective carrier collection and, thus, smaller J_{SC}.

In addition to the thickness of the LVO absorber, the cell performance also sensitively depends on the thickness of the m-TiO_2 layer. Compared with the optimized cell ($t_L = 120$ nm, $t_m = 350$ nm), the cell with the 180-nm m-TiO_2 layer shows a slight increase of V_{OC}. This result is expected because decreasing t_m could reduce the active surface area of the porous structure and, consequently, decrease the recombination rate [71]. However, a less-active interface area also leads to weaker electron collection and, thus, lower J_{SC}. On the other hand, when t_m is far larger than the thickness of LVO penetrating into the m-TiO_2 layer (approximately 300 nm), the photon-generated electrons have to travel long paths before reaching the FTO electrode, which increases the trapping and recombination of electrons. As a consequence, the cell performance degrades as the t_m increases up to 780 and 970 nm.

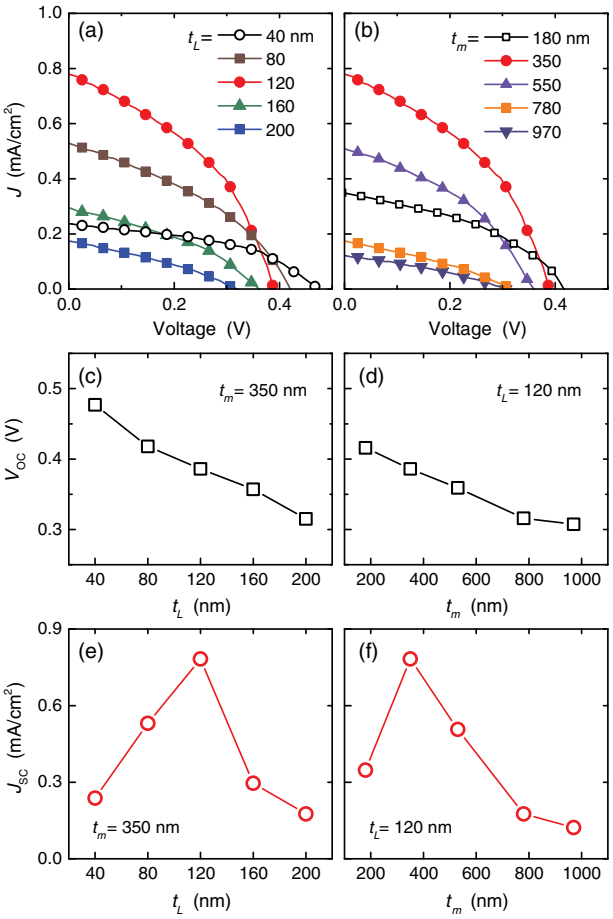

FIG. 10. J-V curves of the m-TiO_2/LVO/spiro-OMeTAD heterojunction solar cells with different thicknesses of (a) LVO layer and (b) m-TiO_2 layer. (c),(d) [(e),(f)] show the evolutions of V_{OC} [J_{SC}] as functions of t_L and t_m, respectively.

E. Discussion

The wide-range solar spectral absorption, along with inherent advantages like long-term stability and an earth abundance of vanadium and lanthanum, makes LVO a promising light-absorbing material for durable and low-cost solar cells. Our systematical characterizations of the m-TiO_2/LVO/spiro-OMeTAD heterojunction solar cells further suggest that the DSSC-type structure is viable for incorporating such strongly correlated electron systems

into photovoltaic devices. Such devices present a short-circuit photocurrent of 0.78 mA/cm^2, an open-circuit voltage of 0.40 V, and a fill factor of 39%. At the same time, our results and analysis identify several challenges for achieving high energy-conversion efficiency using this class of materials.

First, optimizing the sample quality and transport properties of LVO and other TMOs is critical for their potential application in photovoltaic technology. At room temperature, the electron mobility of LVO (0.11 $cm^2\,V^{-1}\,s^{-1}$) is quite low, while its dark carrier density (3.85×10^{19} cm^{-3}) is too high, which are detrimental for producing high photocurrents while suppressing high dark currents. For oxide solar absorbers, it is crucial to precisely control the oxygen stoichiometry and reduce the oxygen-related defects. These extrinsic defects that accumulate during the material preparation are the main source of trapping centers, and the resultant unintentional *n*-type doping contributes to the excessive dark current, limiting the open-circuit voltage. They may also create structural disorders and weaken the *p*-*d* transition-related optical absorption. Therefore, much better control of the growth conditions and development of proper postsynthesis treatments are needed to minimize the extrinsic defects. These improvements on material synthesis could potentially increase the carrier diffusion length and the optimal absorber thickness, thus, improving the charge transport as well as the solar harvesting.

Second, in view of fabricating DSSC-type structures, physical vapor-deposition techniques like PLD, which has been widely used for depositing complex oxide thin films, may not be the most suitable method for preparing Mott insulators for solar-cell applications. As shown in Fig. 8(b), it leads to poor pore filling and inhomogeneous absorber distribution. Replacing the physical vapor depositions by a solution-based sol-gel process, while retaining good crystallinity and low defect density, is clearly a challenge for fabricating oxide-based solar cells. Another promising route is to fabricate high-quality nanoparticles of Mott insulators, since the transport properties can be improved in such single-crystalline nanoparticles, and the active surface areas can be tailored to optimize the carrier transport. Furthermore, the quantum-confinement effect can be utilized to tailor the band gap and light absorption of the nanomaterials of Mott insulators.

Third, despite the optical gap of LVO being as small as 1.1 eV, its indirect nature yields a weak absorption at the band edge. Therefore, for future TMO-based light absorbers, the band gap should be not only optimal for solar harvesting but also direct in nature. A few other TMOs with compatible structures including $BiMnO_3$ (1.1 eV) [39], $YBa_2Cu_3O_6$ (1.5 eV) [72], La_2CuO_4 (1.72 eV), and Sm_2CuO_4 (1.27 eV) [12] could satisfy these two requirements and are worth exploring in the future. Another promising approach is to use narrow-band-gap Mott insulators. Manousakis and co-workers [7,8] theoretically predicted that if the band gap of Mott insulators is reduced to the range of 0.5–1 eV, one energetic photocarrier may produce additional multiple electron-hole pairs through the carrier multiplication process, thus, increasing the quantum efficiency. More research efforts are needed to improve the PCE towards the Shockley-Queisser limit and to study the carrier multiplication in such devices.

Finally, transition-metal oxides offer plenty of opportunities for band-gap engineering through doping or forming superlattices. Recently, Choi *et al.* [73] demonstrated that by site-specific substitution with the Mott insulator lanthanum cobaltite, the band gap of layered ferroelectric bismuth titanate can be narrowed by as much as 1 eV while retaining the ferroelectric property. Furthermore, Assmann *et al.* [9] proposed that the polar order and possible potential gradient in LVO/STO superlattices could be used to separate photon-generated electron-hole pairs. These approaches promote strongly correlated electron systems like Mott insulator LVOs as potential solar materials.

IV. CONCLUSIONS

Our work on LVO is an experimental attempt at using a Mott insulator as a light absorber in solar cells. We systematically investigate the optical absorption and transport properties of LVO films. LVO has a narrow indirect band gap of 1.08 eV, and the *d*-*d* transitions between LHB and UHB and the *p*-*d* transitions between the O 2*p* band and the V 3*d* band give rise to wide-range optical absorption in the solar spectrum. However, because of the presence of high-density charge-trapping defects, the LVO films show unsatisfactory carrier transport ability that hinders the separation, propagation, and collection of electron-hole pairs in photovoltaic devices. Compared to the thin-film device structure, the DSSC-type *m*-TiO_2/LVO/spiro-OMeTAD heterojunctions lead to much improved photovoltaic performances. Our results indicate that the synthesis and transport properties of such transition-metal oxides must be substantially improved in order to increase the power-conversion efficiency. Our research also helps identify several promising approaches such as doping and forming superlattices, through which strong correlated electron systems may find applications in future photovoltaic technologies.

ACKNOWLEDGMENTS

This research is supported by King Abdullah University of Science and Technology. The work at USTC is supported by the National Natural Science Foundation of China under Grants No. 11274287, No. 11474263, and No. U1432251. The work at NREL was funded by the U.S. Department of Energy under Contract No. DE-AC36-08GO28308.

[1] E. Dagotto and Y. Tokura, Strongly correlated electronic materials: Present and future, MRS Bull. **33**, 1037 (2008).

[2] E. Dagotto, Complexity in strongly correlated electronic systems, Science **309**, 257 (2005).

[3] M. Imada, A. Fujimori, and Y. Tokura, Metal-insulator transitions, Rev. Mod. Phys. **70**, 1039 (1998).

[4] J. Zaanen, G. A. Sawatzky, and J. W. Allen, Band Gaps and Electronic Structure of Transition-Metal Compounds, Phys. Rev. Lett. **55**, 418 (1985).

[5] P. A. Lee, N. Nagaosa, and X. G. Wen, Doping a Mott insulator: Physics of high-temperature superconductivity, Rev. Mod. Phys. **78**, 17 (2006).

[6] Y. Tokura, Critical features of colossal magnetoresistive manganites, Rep. Prog. Phys. **69**, 797 (2006).

[7] E. Manousakis, Photovoltaic effect for narrow-gap Mott insulators, Phys. Rev. B **82**, 125109 (2010).

[8] J. E. Coulter, E. Manousakis, and A. Gali, Optoelectronic excitations and photovoltaic effect in strongly correlated materials, Phys. Rev. B **90**, 165142 (2014).

[9] E. Assmann, P. Blaha, R. Laskowski, K. Held, S. Okamoto, and G. Sangiovanni, Oxide Heterostructures for Efficient Solar Cells, Phys. Rev. Lett. **110**, 078701 (2013).

[10] T. Arima and Y. Tokura, Optical study of electronic structure in perovskite-type RMO_3 R = La, Y; M = Sc, Ti, V, Cr, Mn, Fe, Co, Ni, Cu), J. Phys. Soc. Jpn. **64**, 2488 (1995).

[11] T. Arima, Y. Tokura, and J. B. Torrance, Variation of optical gaps in perovskite-type 3*d* transition-metal oxides, Phys. Rev. B **48**, 17006 (1993).

[12] N. N. Kovaleva, A. V. Boris, P. Yordanov, A. Maljuk, E. Brücher, J. Strempfer, M. Konuma, I. Zegkinoglou, C. Bernhard, A. M. Stoneham, and B. Keimer, Optical response of ferromagnetic $YTiO_3$ studied by spectral ellipsometry, Phys. Rev. B **76**, 155125 (2007).

[13] M. D. Scafetta, A. M. Cordi, J. M. Rondinelli, and S. J. May, Band structure and optical transitions in $LaFeO_3$: Theory and experiment, J. Phys. Condens. Matter **26**, 505502 (2014).

[14] M. Nakamura, A. Sawa, J. Fujioka, M. Kawasaki, and Y. Tokura, Interface band profiles of Mott-insulator/$Nb:SrTiO_3$ heterojunctions as investigated by optical spectroscopy, Phys. Rev. B **82**, 201101(R) (2010).

[15] Y. Muraoka, T. Muramatsu, J. Yamaura, and Z. Hiroi, Photogenerated hole carrier injection to $YBa_2Cu_3O_{7-x}$ in an oxide heterostructure, Appl. Phys. Lett. **85**, 2950 (2004).

[16] J. R. Sun, C. M. Xiong, B. G. Shen, P. Y. Wang, and Y. X. Weng, Manganite-based heterojunction and its photovoltaic effects, Appl. Phys. Lett. **84**, 2611 (2004).

[17] K. Zhao, K. J. Jin, H. B. Lu, Y. H. Huang, Q. L. Zhou, M. He, Z. H. Chen, Y. L. Zhou, and G. Z. Yang, Transient lateral photovoltaic effect in *pn* heterojunctions of $La_{0.7}Sr_{0.3}MnO_3$ and Si, Appl. Phys. Lett. **88**, 141914 (2006).

[18] K. X. Jin, Y. F. Li, Z. L. Wang, H. Y. Peng, W. N. Lin, A. K. K. Kyaw, Y. L. Jin, K. J. Jin, X. W. Sun, C. Soci, and T. Wu, Tunable photovoltaic effect and solar cell performance of self-doped perovskite $SrTiO_3$, AIP Adv. **2**, 042131 (2012).

[19] S. Miyasaka, T. Okuda, and Y. Tokura, Critical Behavior of Metal-Insulator Transition in $La_{1-x}Sr_xVO_3$, Phys. Rev. Lett. **85**, 5388 (2000).

[20] R. G. Egdell, M. R. Harrison, M. D. Hill, L. Porte, and G. Wall, A study of the metal-nonmetal transition in lanthanum strontium vanadate by high-resolution electron spectroscopy, J. Phys. C **17**, 2889 (1984).

[21] W. Shockley and H. J. Queisser, Detailed balance limit of efficiency of *p-n* junction solar cells, J. Appl. Phys. **32**, 510 (1961).

[22] Y. Hotta, T. Susaki, and H. Y. Hwang, Polar Discontinuity Doping of the $LaVO_3/SrTiO_3$ Interface, Phys. Rev. Lett. **99**, 236805 (2007).

[23] Y. Hotta, Y. Mukunoki, T. Susaki, and H. Y. Hwang, Growth and epitaxial structure of $LaVO_x$ films, Appl. Phys. Lett. **89**, 031918 (2006).

[24] H. Rotella, U. Lüders, P.-E. Janolin, V. H. Dao, D. Chateigner, R. Feyerherm, E. Dudzik, and W. Prellier, Octahedral tilting in strained $LaVO_3$ thin films, Phys. Rev. B **85**, 184101 (2012).

[25] A. Bera, K. W. Wu, A. Sheikh, E. Alarousu, O. F. Mohammed, and T. Wu, Perovskite oxide $SrTiO_3$ as an efficient electron transporter for hybrid perovskite solar cells, J. Phys. Chem. C **118**, 28494 (2014).

[26] A. D. Sheikh, A. Bera, M. A. Haque, R. B. Rakhi, S. D. Gobbo, H. N. Alshareef, and T. Wu, Atmospheric effects on the photovoltaic performance of hybrid perovskite solar cells, Sol. Energy Mater. Sol. Cells **137**, 6 (2015).

[27] G. Kresse and J. Furthmüller, Efficient iterative schemes for *ab initio* total-energy calculations using a plane-wave basis set, Phys. Rev. B **54**, 11169 (1996).

[28] P. E. Blöchl, Projector augmented-wave method, Phys. Rev. B **50**, 17953 (1994).

[29] B. Adolph, J. Furthmüller, and F. Bechstedt, Optical properties of semiconductors using projector-augmented waves, Phys. Rev. B **63**, 125108 (2001).

[30] G. Y. Gao, S. W. Jin, and W. B. Wu, Lattice-mismatch-strain induced inhomogeneities in epitaxial $La_{0.7}Ca_{0.3}MnO_3$ films, Appl. Phys. Lett. **90**, 012509 (2007).

[31] L. F. Wang, X. L. Tan, P. F. Chen, B. W. Zhi, B. B. Chen, Z. Huang, G. Y. Gao, and W. B. Wu, Annealing assisted substrate coherency and high-temperature antiferromagnetic insulating transition in epitaxial $La_{0.67}Ca_{0.33}MnO_3/NdGaO_3(001)$ films, AIP Adv. **3**, 052106 (2013).

[32] A. David, Y. F. Tian, P. Yang, X. Y. Gao, W. N. Lin, A. B. Shah, J.-M. Zuo, W. Prellier, and T. Wu, Colossal positive magnetoresistance in surface-passivated oxygen-deficient strontium titanite, Sci. Rep. **5**, 10255 (2015).

[33] N. Wang, Q. F. Zhang, and W. Chen, Synthesis and magnetic properties of lanthanum orthovanadate nanorods, Cryst. Res. Technol. **42**, 138 (2007).

[34] N. H. Hur, S. H. Kim, K. S. Yu, Y. K. Park, and J. C. Park, Structural and magnetic properties of the anion-deficient $LaVO_{3-\delta}$, Solid State Commun. **92**, 541 (1994).

[35] H. Rotella, O. Copie, A. Pautrat, P. Boullay, A. David, D. Pelloquin, C. Labbé, C. Frilay, and W. Prellier, Two components for one resistivity in $LaVO_3/SrTiO_3$ heterostructures, J. Phys. Condens. Mater. **27**, 095603 (2015).

[36] G. Silversmit, D. Depla, H. Poelman, G. B. Marin, and R. D. Gryse, Determination of the V 2*p* XPS binding energies for different vanadium oxidation states (V^{5+} to V^{0+}), J. Electron Spectrosc. Relat. Phenom. **135**, 167 (2004).

[37] S. E. Chamberlin, Y. Wang, K. Lopata, T. C. Kaspar, A. W. Cohn, D. R. Gamelin, N. Govind, P. V. Sushko, and S. A. Chambers, Optical absorption and spectral photoconductivity in α-$(Fe_{1-x}Cr_x)_2O_3$ solid-solution thin films, J. Phys. Condens. Matter **25**, 392002 (2013).

[38] P. V. Sushko, L. Qiao, M. Bowden, T. Varga, G. J. Exarhos, R. K. Urban III, D. Barton, and S. A. Chambers, Multiband Optical Absorption Controlled by Lattice Strain in Thin-Film $LaCrO_3$, Phys. Rev. Lett. **110**, 077401 (2013).

[39] X. S. Xu, J. F. Ihlefeld, J. H. Lee, O. K. Ezekoye, E. Vlahos, R. Ramesh, V. Gopalan, X. P. Pan, D. G. Schlom, and J. L. Musfeldt, Tunable band gap in $Bi(Fe_{1-x}Mnx)O_3$ films, Appl. Phys. Lett. **96**, 192901 (2010).

[40] B. S. Holinsworth, D. Mazumdar, H. Sims, Q.-C. Sun, M. K. Yurtisigi, S. K. Sarker, A. Gupta, W. H. Butler, and J. L. Musfeldt, Chemical tuning of the optical band gap in spinel ferrites: $CoFe_2O_4$ vs $NiFe_2O_4$, Appl. Phys. Lett. **103**, 082406 (2013).

[41] Q.-C. Sun, H. Sims, D. Mazumdar, J. X. Ma, B. S. Holinsworth, K. R. O'Neal, G. Kim, W. H. Butler, A. Gupta, and J. L. Musfeldt, Optical band gap hierarchy in a magnetic oxide: Electronic structure of $NiFe_2O_4$, Phys. Rev. B **86**, 205106 (2012).

[42] A. Walsh, J. L. F. DaSilva, S. H. Wei, C. Körber, A. Klein, L. F. J. Piper, A. DeMasi, K. E. Smith, G. Panaccione, P. Torelli, D. J. Payne, A. Bourlange, and R. G. Egdell, Nature of the Band Gap of In_2O_3 Revealed by First-Principles Calculations and X-Ray Spectroscopy, Phys. Rev. Lett. **100**, 167402 (2008).

[43] Y. F. Li, W. J. Yin, R. Deng, R. Chen, J. Chen, Q. Y. Yan, B. Yao, H. D. Sun, S. H. Wei, and T. Wu, Realizing a SnO_2-based ultraviolet light-emitting diode via breaking the dipole-forbidden rule, NPG Asia Mater. **4**, e30 (2012).

[44] M. Rohlfing and S. G. Louie, Electron-hole excitations and optical spectra from first principles, Phys. Rev. B **62**, 4927 (2000).

[45] X. B. Chen, L. Lu, P. Y. Yu, and S. S. Mao, Increasing solar absorption for photocatalysis with black hydrogenated titanium dioxide nanocrystals, Science **331**, 746 (2011).

[46] G. J. Snyder, R. Hiskes, S. DiCarolis, M. R. Beasley, and T. H. Geballe, Intrinsic electrical transport and magnetic properties of $La_{0.67}Ca_{0.33}MnO_3$ and $La_{0.67}Sr_{0.33}MnO_3$ MOCVD thin films and bulk material, Phys. Rev. B **53**, 14434 (1996).

[47] K. Maiti, N. Y. Vasanthacharya, and D. D. Sarma, Doping dependence of transport and magnetic properties in $La_{1-x}Ca_xVO_3$, J. Phys. Condens. Matter **9**, 7507 (1997).

[48] R. K. Zheng, A. N. Tang, Y. Yang, W. Wang, G. Li, X. G. Li, and H. C. Ku, Transport, magnetic, specific heat, internal friction, and shear modulus in the charge ordered $La_{0.25}Ca_{0.75}MnO_3$ manganite, J. Appl. Phys. **94**, 514 (2003).

[49] S. Ono, S. Komiya, and Y. Ando, Strong charge fluctuations manifested in the high-temperature Hall coefficient of high-T_c cuprates, Phys. Rev. B **75**, 024515 (2007).

[50] D. Ruzmetov, D. Heiman, B. B. Claflin, V. Narayanamurti, and S. Ramanathan, Hall carrier density and magnetoresistance measurements in thin-film vanadium dioxide across the metal-insulator transition, Phys. Rev. B **79**, 153107 (2009).

[51] J. Nelson, *The Physics of Solar Cells* (Imperial College-Press, London, 2003).

[52] A. Luque and S. Hegedus, *Handbook of Photovoltaic Science and Engineering* (John Wiley & sons Ltd., Chichester, 2003).

[53] V. D. Mihailetchi, J. K. J. van Duren, P. W. M. Blom, J. C. Hummelen, R. A. J. Janssen, J. M. Kroon, M. T. Rispens, W. J. H. Verhees, and M. M. Wienk, Electron transport in methanofullerene, Adv. Funct. Mater. **13**, 43 (2003).

[54] W. Gong, H. Yun, Y. B. Ning, J. E. Greedan, W. R. Datars, and C. V. Stager, Oxygen-deficient $SrTiO_{3-x}$, $x = 0.28$, 0.17, and 0.08. Crystal growth, crystal structure, magnetic and transport properties, J. Solid State Chem. **90**, 320 (1991).

[55] X. F. Hao, Z. M. Wang, M. Schmid, U. Diebold, and C. Franchini, Coexistence of trapped and free excess electrons in $SrTiO_3$, Phys. Rev. B **91**, 085204 (2015).

[56] J. T. Devreese, S. N. Klimin, J. L. M. Van Mechelen, and D. van der Marel, Many-body large polaron optical conductivity in $SrTi_{1-x}Nb_xO_3$, Phys. Rev. B **81**, 125119 (2010).

[57] Y. Yamada, H. K. Sato, Y. Hikita, H. Y. Hwang, and Y. Kanemitsu, Measurement of the Femtosecond Optical Absorption of $LaAlO_3/SrTiO_3$ Heterostructures: Evidence for an Extremely Slow Electron Relaxation at the Interface, Phys. Rev. Lett., **111**, 047403 (2013).

[58] T. Kohmoto, D. Ikeda, X. Liang, and T. Moriyasu, Direct observation of the spatial and temporal dynamics of polaron diffusion in $SrTiO_3$, Phys. Rev. B **87**, 214301 (2013).

[59] M. Rosi and C. Pelosi, The potential of III-V semiconductors as terrestrial photovoltaic devices, Prog. Photovoltaics **15**, 51 (2007).

[60] K. L. Chopra, P. D. Paulson, and V. Dutta, Thin film solar cells: An overview, Prog. Photovoltaics **12**, 69 (2004).

[61] C. Wang, K. J. Jin, R. Q. Zhao, H. B. Lu, H. Z. Guo, C. Ge, M. He, C. Wang, and G. Z. Yang, Ultimate photovoltage in perovskite oxide heterostructures with critical film thickness, Appl. Phys. Lett. **98**, 181101 (2011).

[62] M. Grätzel, Dye-sensitized solar cells, J. Photochem. Photobiol. C **4**, 145 (2003).

[63] A. Hagfeldt, G. Boschloo, L. Sun, L. Kloo, and H. Pettersson, Dye-sensitized solar cells, Chem. Rev. **110**, 6595 (2010).

[64] J. A. Chang, S. H. Im, Y. H. Lee, H. J. Kim, C. S. Lim, J. H. Heo, and S. I. Seok, Panchromatic photon-harvesting by hole-conducting materials in inorganic-organic heterojunction sensitized-solar cell through the formation of nanostructured electron channels, Nano Lett. **12**, 1863 (2012).

[65] P. V. Kamat, Quantum dot solar cells. Semiconductor nanocrystals as light harvesters, J. Phys. Chem. C **112**, 18737 (2008).

[66] M. M. Lee, J. Teuscher, T. Miyasaka, T. N. Murakami, and H. J. Snaith, Efficient hybrid solar cells based on meso-superstructured organometal halide perovskites, Science **338**, 643 (2012).

[67] G. Herrera, E. Chavira, J. Jiménez-Mier, A. Ordoñez, E. Fregoso-Israel, L. Baños, E. Bucio, J. Guzmán, O. Novelo, and C. Flores, Structural and morphology comparison between m-$LaVO_4$ and $LaVO_3$ compounds prepared by sol–gel acrylamide polymerization and solid state reaction, J. Alloys Compd. **479**, 511 (2009).

[68] J. H. Heo, S. H. Im, J. H. Noh, T. N. Mandal, C.-S. Lim, J. A. Chang, Y. H. Lee, H. Kim, A. Sarkar, M. K. Nazeeruddin, M. Grätzel, and S. I. Seok, Efficient inorganic-organic hybrid heterojunction solar cells containing perovskite compound and polymeric hole conductors, Nat. Photonics **7**, 486 (2013).

[69] H. J. Snaith, L. Schmidt-Mende, and M. Grätzel, Light intensity, temperature, and thickness dependence of the open-circuit voltage in solid-state dye-sensitized solar cells, Phys. Rev. B **74**, 045306 (2006).

[70] J. A. Barker, C. M. Ramsdale, and N. C. Greenham, Modeling the current-voltage characteristics of bilayer polymer photovoltaic devices, Phys. Rev. B **67**, 075205 (2003).

[71] P. P. Boix, Y. H. Lee, F. F. Santiago, S. H. Im, I. M. Sero, J. Bisquert, and S. I. Seok, From flat to nanostructured photovoltaics: Balance between thickness of the absorber and charge screening in sensitized solar cells, ACS Nano, **6**, 873 (2012).

[72] G. Yu, C. H. Lee, D. Mihailovic, A. J. Heeger, C. Fincher, N. Herron, and E. M. McCarron, Photoconductivity in insulating $YBa_2Cu_3O_{6+x}$: From Mott-Hubbard insulator to Fermi glass via oxygen doping, Phys. Rev. B **48**, 7545 (1993).

[73] W. S. Choi, M. F. Chisholm, D. J. Singh, T. Choi, G. E. Jellison, Jr, and H. N. Lee, Wide bandgap tunability in complex transition metal oxides by site-specific substitution, Nat. Commun. **3**, 689 (2012).